RESEARCH ARTICLE

ADVANCED FUNCTIONAL MATERIALS
www.afm-journal.de

Promoting Reaction Kinetics and Boosting Sodium Storage Capability via Constructing Stable Heterostructures for Sodium-Ion Batteries

Chunrong Ma, Xiao Tang, Haoxi Ben, Wei Jiang, Xinyu Shao, Guoxiu Wang, and Bing Sun**

Constructing heterostructures containing multiple active components is proven to be an efficient strategy for enhancing the sodium storage capability of anode materials in sodium-ion batteries (SIBs). However, performance enhancement is often attributed to the unclear synergistic effects among the active components. A comprehensive understanding of the reaction mechanisms on the interfaces at the atomic level remains elusive. Herein, the carbon-coated Fe_3Se_4/CoSe (Fe_3Se_4/CoSe-C) anode material as a model featuring atomic-scale contact interfaces is synthesized. This unique heterogeneous architecture offers an adjustable electronic structure, which facilitates rapid reaction kinetics and enhances structural integrity. In situ microscopic and ex situ spectral characterization techniques, along with theoretical simulations, confirm that the heterointerface with strong electric fields promotes Na^+ ion migration. Based on solid-state nuclear magnetic resonance (NMR) analysis, an interface charge storage mechanism is revealed, resulting in the enhanced specific capacity of the anode materials. When employed as an anode in SIBs, the Fe_3Se_4/CoSe-C electrode demonstrates excellent rate capabilities (218 mAh g^{-1} at 7 A g^{-1}) and prolonged cycling stability (258 mAh g^{-1} at 5 A g^{-1} after 1000 cycles). This work highlights the significance of heterointerface engineering in electrode material design for rechargeable batteries.

1. Introduction

The development of sodium-ion batteries (SIBs) as viable alternatives to lithium-ion batteries (LIBs) has garnered significant interest due to the abundance of sodium resources and operational similarities. However, one of the main challenges hindering the commercialization of SIBs is the lower energy density and power density compared to LIBs, primarily stemming from performance limitations in electrode materials, especially anode materials.[1–5] To overcome these challenges, extensive research efforts have been devoted to exploring various anode materials, such as nanostructured carbonaceous materials,[6–11] metal alloys,[12–15] and metal oxides/sulfides,[16–19] et al. Among these anode materials, transition metal selenides (TMSs) have emerged as promising candidates due to their abundant resources, diverse electronic properties, and high specific capacity. Additionally, the larger atomic radius of selenium weakens the metal-selenium bonds compared to their metal–oxygen and metal–sulfur counterparts, thereby enhancing the efficiency of the conversion reaction in the selenides.[16,20] However, despite these advantages, TMSs still need to overcome several challenges, such as significant volume expansion and sluggish reaction kinetics during charge and discharge cycles, leading to quick capacity degradation and suboptimal rate performance.[21] The most common approach to addressing these challenges is to restructure the active materials

---

C. Ma, H. Ben, W. Jiang, X. Shao
College of Textiles & Clothing
Key Laboratory of Bio-Fibers and Eco-Textiles
Qingdao University
Qingdao, Shandong 266071, China

X. Tang
School of Chemistry and Chemical Engineering
Qingdao University
Qingdao, Shandong 266071, China

G. Wang, B. Sun
Centre for Clean Energy Technology
School of Mathematical and Physical Sciences
Faculty of Science
University of Technology Sydney
Ultimo, NSW 2007, Australia
E-mail: guoxiu.wang@uts.edu.au; bing.sun@uts.edu.au

The ORCID identification number(s) for the author(s) of this article can be found under https://doi.org/10.1002/adfm.202412879

DOI: 10.1002/adfm.202412879

into nanoscale dimensions and incorporate them with conductive carbon materials.[22–26] Reducing the primary particle sizes of TMSs enhances the structure integrity upon cycling. The incorporation of carbonous materials serves to confine the volume expansion of TMSs during cycling and maintain electrical connectivity, thereby improving electrochemical performance. However, despite these improvements, achieving both high reversible capacity and long-term cycling stability remains a significant challenge in developing high-performance anode materials for SIBs.

Recent studies have confirmed that constructing electrode materials with heterostructures is a highly effective approach to significantly enhance the Na^+ ion storage performance in TMSs.[27] This enhancement arises from synergistic effects wherein components mutually reinforce or modify each other, thereby alleviating the shortcomings inherent in individual constituents.[28–31] Creating heterostructures with different bandgaps can enhance surface reaction kinetics and facilitate charge transfer.[32–34] Currently, most research works primarily focus on exploring the enhanced kinetic properties of heterostructure, overlooking the evolution of material structure. However, stress variations, which persist within the heterogeneous structure during the charge/discharge process, can lead to significant volume expansion, exacerbating the likelihood of fracture at the heterogeneous interface, particularly if the bonding strength is weak. Consequently, the potential benefits associated with heterogeneous structures may be compromised or completely lost. Hence, ensuring the structural integrity of heterostructure materials remains a critical challenge. Besides enhanced reaction kinetics, heterostructure electrodes often demonstrate increased specific capacity, even surpassing theoretical values.[35–37] However, the underlying reasons for this enhanced capacity have not received much attention. Most studies merely attribute it to unspecified synergies without delving into the nature of these synergistic effects. Thus, more efforts are needed to investigate the underlying reaction mechanisms and the interface interactions governing the performance enhancement of heterostructures.

Herein, we present an innovative in situ approach for fabricating a Fe_3Se_4/CoSe heterostructure embedded within hierarchically interconnected carbon frameworks (Fe_3Se_4/CoSe-C) as an anode in SIBs. This unique structure, featuring nanoscale heterointerfaces, effectively mitigates internal mechanical force changes, thereby preventing uncontrolled structural damage. Through electronic structure regulation, the sodiation/desodiation and reconversion kinetics are simultaneously enhanced. Contrasted with the ambiguous synergistic effect, we found that the interface between Fe_3Se_4 and CoSe can offer additional active sites for Na^+ ion storage, leading to an increased specific capacity. Additionally, density functional theory (DFT) calculations indicate that the fast kinetics and enhanced rate performance stem from the built-in electric field at the heterointerfaces, which significantly lowers Na^+ diffusion barriers and expedites charge transfer.

2. Results and Discussion

The Fe_3Se_4/CoSe-C anode material was synthesized via a sol-gel method followed by a selenization process, as illustrated in **Figure** 1a. Sodium alginate (SA) solution was slowly added into a solution containing Co^{2+} and Fe^{3+} precursors to form a Fe/Co-alginate hydrogel with Co^{2+}/Fe^{3+} cations coordinated with G-block in SA. Subsequently, through a freeze-drying process, a porous precursor was obtained. Then, the Fe_3Se_4/CoSe-C heterostructure encapsulated into an interconnected carbon framework was obtained via the high-temperature gas-phase selenizing reaction with the introduction of the selenium vapor into a quartz-tube reactor.[38] Reference samples of carbon-coated Fe_3Se_4 nanoparticles (Fe_3Se_4-C) and carbon-coated CoSe nanoparticles (CoSe-C) were also prepared using the same method.

The morphologies and microstructures of the synthesized materials were examined using scanning electron microscopy (SEM) and transmission electron microscopy (TEM). As shown in Figure 1b, the Fe_3Se_4/CoSe-C heterostructure exhibits a typical 3D hierarchical porous structure. The highly conductive carbon nanotubes are interlaced into a porous framework, facilitating fast ion/electron transport for rapid reaction kinetics. The TEM image in Figure 1c indicates that the Fe_3Se_4/CoSe nanoparticles are uniformly dispersed in the carbon matrix without obvious aggregation. Notably, the high-resolution TEM (HRTEM) image in Figure 1d reveals the Fe_3Se_4/CoSe nanoparticles are tightly wrapped by continuous graphitic carbon layers. The resulting graphitic carbon is converted from amorphous carbon, which is catalyzed by Co and Fe particles in situ formed at high temperatures. Amorphous carbons were also formed among the Fe_3Se_4/CoSe-C nanoparticles, creating a unique conductive network and contributing to excellent electronic conductivity. The HRTEM of Fe_3Se_4/CoSe-C (Figure 1e) exhibits distinct lattice fringes with interplanar spacings of 0.27 and 0.54 nm, corresponding to the (101) plane of CoSe and (101) Fe_3Se_4, respectively.[39,40] Such intimate lattice contacts between CoSe and Fe_3Se_4 indicate a well-constructed heterointerface. Additionally, more HRTEM images have been provided to further substantiate the existence of the heterostructures (Figure S1, Supporting Information). Energy dispersive X-ray spectroscopy (EDS) reveals the uniform elemental distribution of Fe, Co, Se and C in the Fe_3Se_4/CoSe-C heterostructure (Figure S2, Supporting Information). The carbon content in the Fe_3Se_4/CoSe-C composite is ≈17%, which is calculated based on thermogravimetric analysis (TGA) results in Figure S3 (Supporting Information).

The crystal structure of the synthesized samples was analyzed through X-ray diffraction (XRD). As shown in Figure 1f, the detected peaks in the Fe_3Se_4/CoSe-C heterostructure are well-matched with Fe_3Se_4 (PDF no. 71–2250) and CoSe (PDF no. 89–2004), indicating the high purity of the as-prepared samples. Notably, a broad peak at ≈23° corresponds to carbon. Additionally, the crystal structure of individual Fe_3Se_4 and CoSe was analyzed separately, and the corresponding XRD patterns are demonstrated in Figure S4 (Supporting Information). The surface chemical composition and valence states of the Fe_3Se_4/CoSe-C heterostructure were investigated by X-ray photoelectron spectroscopy (XPS). The XPS spectrum of Fe_3Se_4/CoSe-C is depicted in Figure S5a (Supporting Information), revealing characteristic peaks of Fe, Co, Se, and C elements, consistent with the EDS results. Regarding the high-resolution Fe 2p spectrum (Figure 1g), the peaks at binding energies of 710.3 and 724.2 eV are attributed to Fe^{2+} $2p_{3/2}$ and Fe^{2+} $2p_{1/2}$, respectively.[41] Additionally, the peaks at 712.4 and 725.3 eV represent characteristic peaks of Fe^{3+} $2p_{3/2}$ and Fe^{3+} $2p_{1/2}$. Two satellite peaks centered at 719.1 and

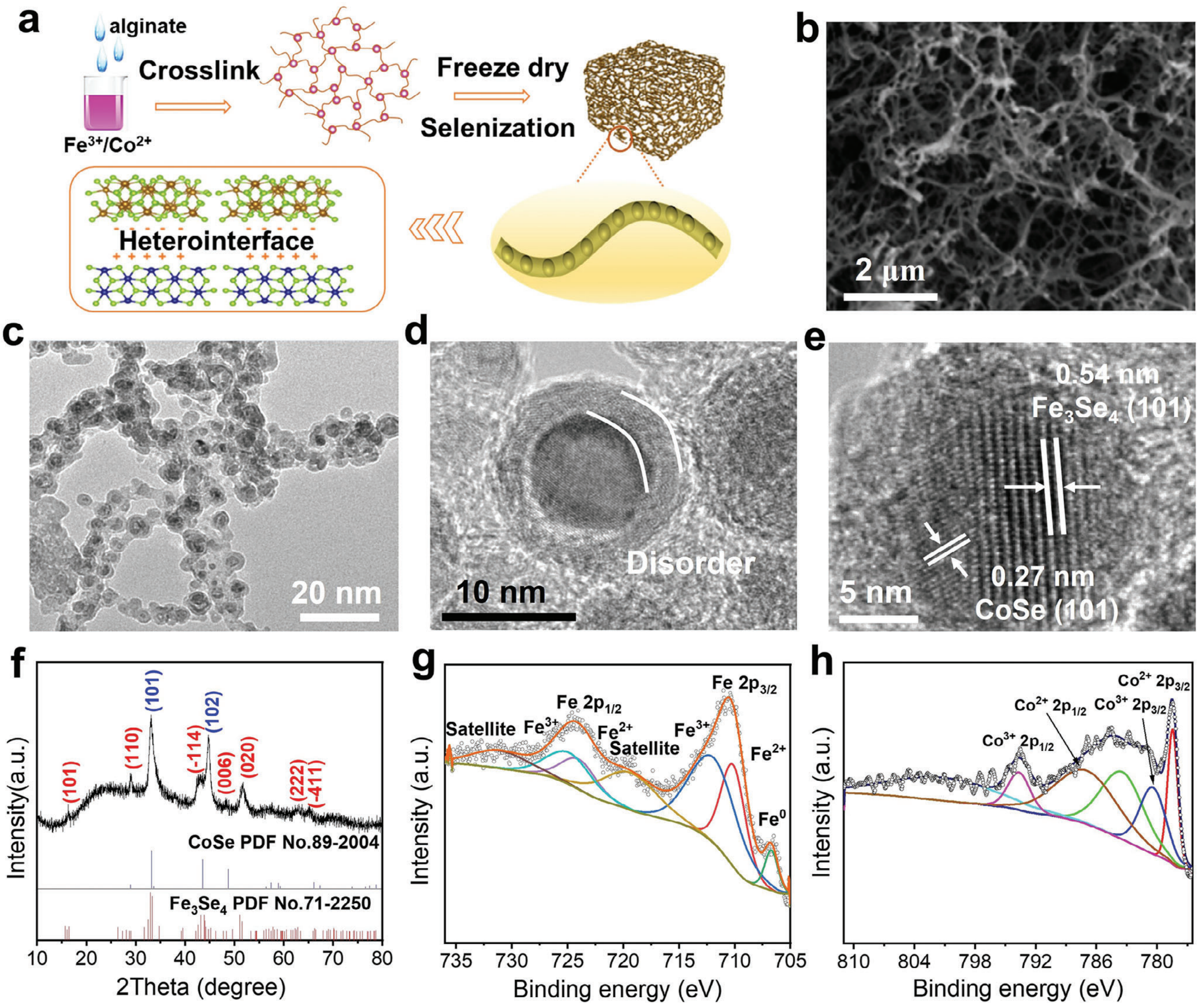

Figure 1. a) Schematic illustration for the synthesis of Fe_3Se_4/CoSe-C. b) SEM image of Fe_3Se_4/CoSe-C. c,d) TEM images of Fe_3Se_4/CoSe-C at different magnifications. e) HRTEM image of Fe_3Se_4/CoSe-C. f) XRD pattern of Fe_3Se_4/CoSe-C. g,h) High-resolution XPS spectra of Fe 2p and Co 2p for Fe_3Se_4/CoSe-C.

731.2 eV, consistent with previous literature.[42] Moreover, a peak corresponding to Fe^0 at 707.35 eV indicates a slight reduction of Fe^{3+} during the pyrolysis process. Compared with the Fe 2p spectrum of Fe_3Se_4-C in Figure S6a (Supporting Information), the main peaks of Fe 2p in the Fe_3Se_4/CoSe-C composite shift toward higher binding energies, which is due to the spontaneous formation of heterojunctions between Fe_3Se_4 and CoSe, leading to an increase in electron density around Co and a decrease around Fe. In addition, the high-resolution spectral analysis of Co 2p reveals four different peaks, as shown in Figure 1h. Two characteristic peaks at the binding energies of 778.4 and 787.5 eV are attributed to Co^{2+} $2p_{3/2}$ and Co^{2+} $2p_{1/2}$, respectively, while the peaks at 780.3 and 793.7 eV correspond to Co^{3+} $2p_{3/2}$ and Co^{3+} $2p_{1/2}$.[43] Due to the orbital relationship between Co atoms and Se atoms, two satellite peaks are observed as well. Compared with the Co 2p spectrum of CoSe-C in Figure S6b (Supporting Information), the main peaks of Co 2p in Fe_3Se_4/CoSe-C composites shift toward a lower binding energy. In the high-resolution Se 3d spectra (Figure S5b, Supporting Information), two distinct characteristic peaks at 55.88 and 54.08 eV are attributed to Se $3d_{3/2}$ and Se $3d_{5/2}$, respectively, and a wide peak at 59.03 eV can be interpreted as the peak of SeO_x.[44] The high-resolution spectral fitting analysis of C1s in Figure S5c (Supporting Information) reveals three peaks corresponding to C—C, C—O, and C═O bonds, respectively. The Raman spectrum displayed in Figure S5d (Supporting Information) reveals two significant peaks at 1347 and 1587 cm^{-1}, corresponding to the D mode (sp3 C, indicative of defects) and the G mode (sp2 graphite carbon), respectively. The I_D/I_G ratio, which indicates the carbon's disorder degree,[45] is measured at 1.18 based on the Raman analysis. This ratio points to an amorphous structure with a higher number of defects in the carbon matrix of the Fe_3Se_4/CoSe-C composite.

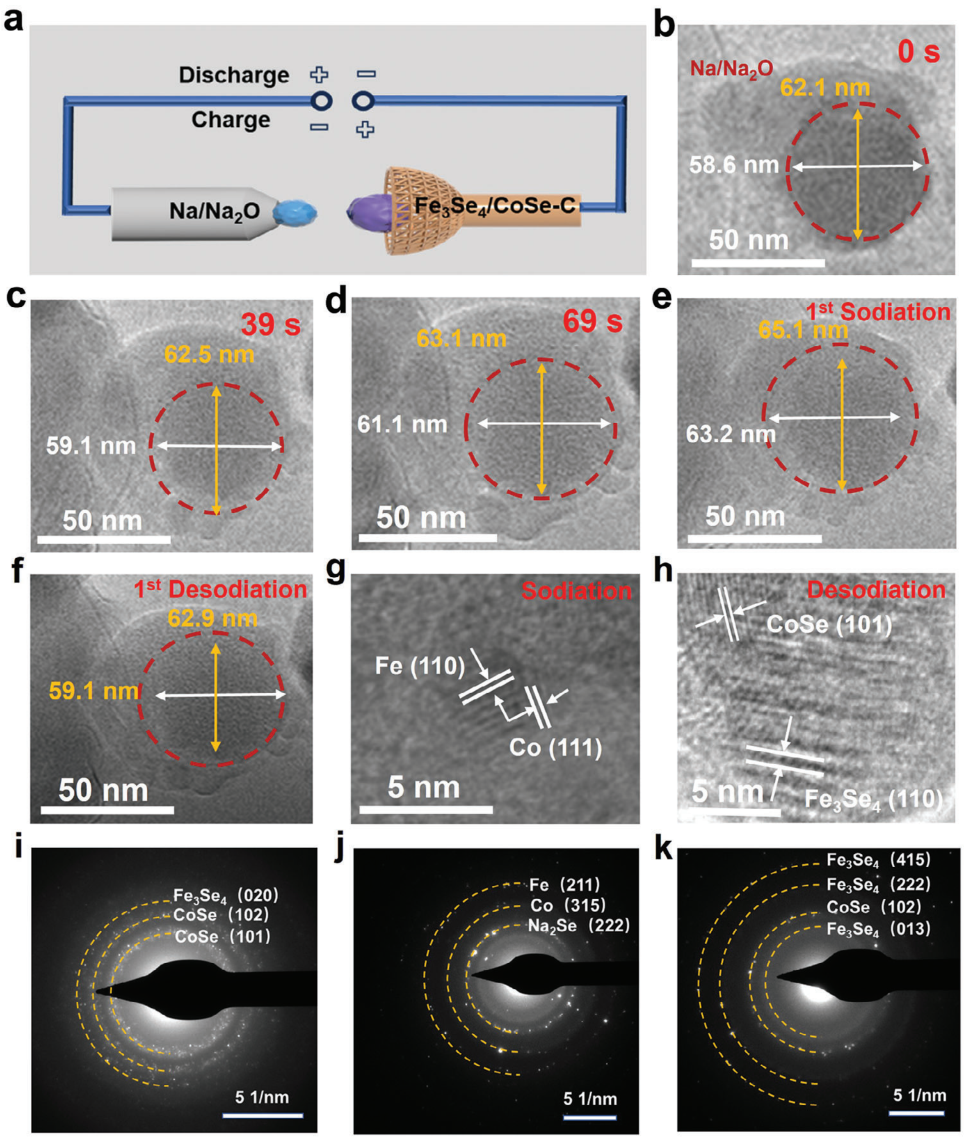

Figure 2. a) Schematic illustration of a nanocell for in situ TEM characterization. b–e) Time-lapse TEM images of Fe$_3$Se$_4$/CoSe-C during the first sodiation process. f) Time-lapse TEM image of Fe$_3$Se$_4$/CoSe-C at the desodiation state. g) Ex situ HRTEM image of Fe$_3$Se$_4$/CoSe-C discharged to 0.01 V. h) Ex situ HRTEM image of Fe$_3$Se$_4$/CoSe-C charged to 3.0 V. i–k) SEAD patterns of Fe$_3$Se$_4$/CoSe-C i) acquired at origin state, j) after discharged to 0.01 V, and k) after charged to 3.0 V.

The structural evolution of the constructed heterogeneous structure during the sodiation and desodiation processes was first investigated using in situ TEM techniques (**Figure** 2a–f). The corresponding schematic of the nanocell for TEM characterization is depicted in Figure 2a. Additionally, time-resolved TEM was utilized to dynamically capture the morphological changes of the Fe$_3$Se$_4$/CoSe-C electrode during sodium insertion/extraction processes, with the corresponding videos presented in the supporting information. Under the voltage of −3.0 V (i.e., Na$^+$ ion insertion condition), the structure of the Fe$_3$Se$_4$/CoSe-C heterostructure remains stable with no significant volume expansion. Only slight dimensional growth is observed, as demonstrated in various frames of the video. At 39 s of the sodium insertion process (Figure 2c), the longitudinal dimension increased from 62.1 to 62.5 nm, and the transverse dimension increased from 58.6 to 59.1 nm. The continuous sodium insertion results in the increase of longitudinal and transverse dimensions to 63.1 and 61.1 nm at 69 s, respectively (Figure 2d). At the fully sodiation stage, the transverse and longitudinal dimensions of the Fe$_3$Se$_4$/CoSe-C nanoparticle only slightly increased to 63.2 and 65.1 nm, respectively (Figure 2e), close to the original dimensions. During the following desodiation process, the transverse and longitudinal dimensions of the Fe$_3$Se$_4$/CoSe-C nanoparticle decreased to 59.1 and 62.9 nm, respectively (Figure 2f). The constructed heterojunctions inside the Fe$_3$Se$_4$/CoSe-C nanoparticle remain intact without obvious rupture or fragmentation throughout the entire sodiation and desodiation processes, fully leveraging their advantages during the charge and discharge processes.

For further ex situ HRTEM observation, at the full sodiation stage, the HRTEM image in Figure 2g reveals lattice fringes with interplanar distances of 0.245 and 0.27 nm, which are attributed to the Fe (110) and Co (111) planes, respectively. In addition, complete sodium extraction leads to the re-emergence of CoSe and Fe_3Se_4 lattice (Figure 2h), confirming the excellent reversibility of the as-prepared heterostructure. Further evidence to identify the discharge products (i.e., Na_2Se, Co, and Fe) is provided by diffraction rings in selected area electron diffraction (SAED) patterns, as shown in Figure 2i,j. After charging the Fe_3Se_4/CoSe-C electrode to 3.0 V, the reappearance of CoSe and Fe_3Se_4 phases can be detected, as shown in Figure 2k.

The sodium storage performances of the Fe_3Se_4/CoSe-C electrode were evaluated in coin cells. The cyclic voltammetry (CV) curves of the Fe_3Se_4/CoSe-C electrode obtained at a scanning rate of 0.1 mV s^{-1} are shown in Figure S7a (Supporting Information). During the first discharge process, a small reduction peak at ≈1.2 V is observed, which is attributed to Na^+ insertion into Fe_3Se_4 and CoSe.[23,39,46] The broad peaks located at ≈0.5 V are related to the reduction of Na_xCoSe and $Na_xFe_3Se_4$ to metal Co and Fe, respectively. During the oxidation process, oxidation peaks appear ≈1.48, 1.62, and 1.82 V, which are related to the formation of Fe_3Se_4 and CoSe. Subsequent cathodic and anodic scanning processes reveal consistent shapes in the CV curves, with no significant deviation observed in the oxidation and reduction peaks. This suggests that the Fe_3Se_4/CoSe-C electrode exhibits excellent reversibility and stability after the first cycle. For comparison, the CV profiles of the Fe_3Se_4-C and CoSe-C electrodes were also evaluated (Figure S7b,c, Supporting Information).

The constant current charge and discharge test was conducted within a voltage range of 0.01–3.0 V. At low current density, the Fe_3Se_4/CoSe-C electrode exhibited high initial discharge and charge capacities of 576 and 466 mAh g^{-1}, respectively, corresponding to a Coulombic efficiency of ≈81% in the first cycle (Figure S8a, Supporting Information), which is comparable to the state-of-the-art hard carbon materials (Table S1, Supporting Information). The initial capacity loss primarily stemmed from electrolyte decomposition and SEI formation. For comparison, the charge–discharge voltage curves of Fe_3Se_4-C and CoSe-C electrodes were also shown in Figure S8b,c (Supporting Information). Both of these samples displayed lower specific capacities compared to the Fe_3Se_4/CoSe-C electrode. Furthermore, the cycling performance of the Fe_3Se_4/CoSe-C, Fe_3Se_4-C, and CoSe-C electrodes was evaluated at a current density of 1 A g^{-1}. The cells were activated by cycling at a low current density of 0.2 A g^{-1} for the first five cycles. As depicted in **Figure 3**a, the Fe_3Se_4/CoSe-C electrode demonstrated the highest specific capacity of ≈400 mAh g^{-1} at the 100th cycle, surpassing that of both the Fe_3Se_4-C and CoSe-C electrodes. The rate capabilities of the electrodes were evaluated at different current densities ranging from 0.2 to 7 A g^{-1} (Figure 3b). As the current densities increase from 0.2 to 5 A g^{-1}, the specific capacities of the Fe_3Se_4/CoSe-C electrode decrease from 485 to 239 mAh g^{-1}. At the higher current density of 7 A g^{-1}, the Fe_3Se_4/CoSe-C electrode still maintains a reversible specific capacity of 218 mAh g^{-1}. Remarkably, upon returning to the low current density of 0.2 A g^{-1}, the corresponding specific capacity rebounds to 474 mAh g^{-1}. In contrast, the Fe_3Se_4-C and CoSe-C electrodes demonstrate reduced capacities across all corresponding current densities. The excellent rate performance of the Fe_3Se_4/CoSe-C electrode is primarily attributed to the formation of a heterojunction at the Fe_3Se_4/CoSe phase boundary, which enhances the reaction kinetics. The long-term cycling performance is a critical parameter for evaluating SIBs. Therefore, the long-term cycling stability of the Fe_3Se_4/CoSe-C electrode was investigated at a high current density of 5 A g^{-1}, as depicted in Figure 3c. Notably, after 1000 cycles, the specific capacity of the Fe_3Se_4/CoSe-C composite remains at ≈258 mAh g^{-1}, indicating its excellent cycling stability. The capacity retention rate after 1000 cycles is 89%, which corresponds to a capacity loss of ≈0.011% per cycle. Such excellent cycling stability can be attributed to the unique combination of Fe_3Se_4 and CoSe, which enhances the overall structural stability of the electrode and prevents significant degradation during repeated charge-discharge processes. Additionally, the incorporation of a carbon matrix helps buffer the volume changes during cycling, maintaining the electrode's mechanical integrity and preventing pulverization. The performance comparison in Figure S2 (Supporting Information) further demonstrates the superior properties of the as-prepared Fe_3Se_4/CoSe-C.

To better understand the Na^+ diffusion kinetics in Fe_3Se_4/CoSe-C, Fe_3Se_4-C and CoSe-C electrodes, galvanostatic intermittent titration technique (GITT) tests were performed. As shown in Figure 3d, the GITT curve of the Fe_3Se_4/CoSe-C electrode was obtained after constant current pulse discharge/charge for 0.5 h at the current density of 0.1 A g^{-1} and then standing for 1 h. The diffusion coefficient of sodium ion (D_{Na^+}) can be calculated according to the following formula (the details are shown in Figure S9, Supporting Information):[47]

$$D_{Na^+} = \frac{4}{\pi\tau}\left(\frac{m_B V_M}{M_B A}\right)^2\left(\frac{\Delta E_S}{\Delta E_t}\right)^2 \tag{1}$$

During the discharge and charge process, the diffusion coefficient of the Fe_3Se_4/CoSe-C electrode is higher than that of Fe_3Se_4-C and CoSe-C electrodes (Figure 3e; Figure S10, Supporting Information), which indicates that Na^+ ion diffuses more easily in Fe_3Se_4/CoSe-C electrode.

To further understand the Na^+ ion storage mechanisms in Fe_3Se_4/CoSe-C electrode, CV tests were further performed at different scan rates (Figure 3f). When the scan rate increases from 0.1 to 2.0 mV s^{-1}, all CV curves show similar peak positions and peak shapes. The relationship between current (i) and scan rate (v) can be expressed by the following formula:[48]

$$i = av^b \tag{2}$$

where i is the current density, v is the scanning rate, and a and b are constants. The value of b can be obtained by calculating the slopes of $log(i)$ and $log(v)$. A b value of 0.5 indicates that the charge storage process is controlled by the diffusion behavior, while a b value of 1.0 indicates that the capacitor behavior controls the entire process. Figure 3g shows the b values at the corresponding potential during the discharge process, all of which are higher than 0.7. These results show that the sodium storage behavior in the Fe_3Se_4/CoSe-C electrode is mainly due to the pseudocapacitance behavior with fast kinetic feature. In order to quantify the contribution rate of capacitance behavior in the

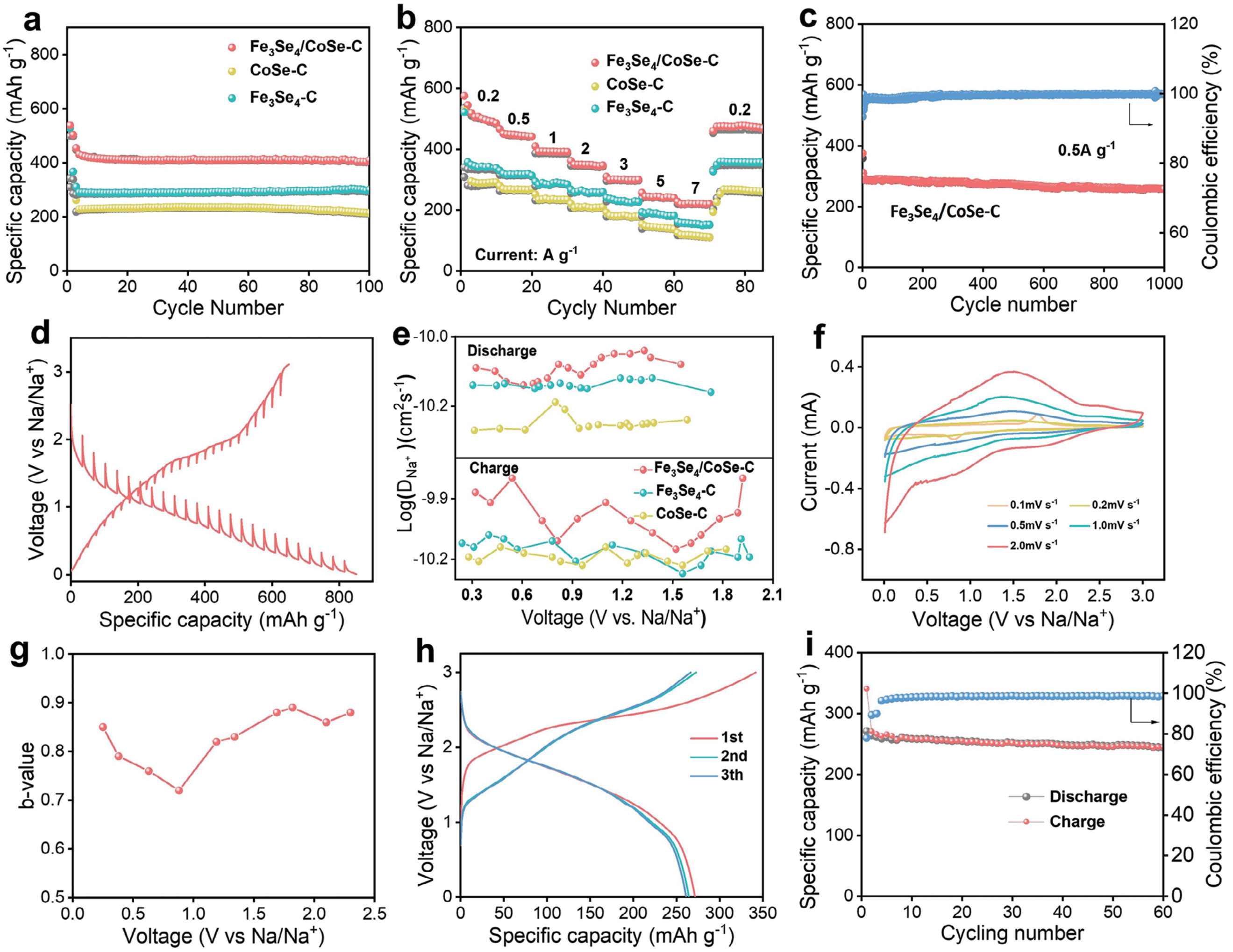

Figure 3. a) The cycling performance of Fe$_3$Se$_4$-C, CoSe-C, and Fe$_3$Se$_4$/CoSe-C electrodes at 1 A g^{-1}. b) Rate performances of Fe$_3$Se$_4$-C, CoSe-C, and Fe$_3$Se$_4$/CoSe-C electrodes at various currents ranging from 0.2 to 7 A g^{-1}. c) The long-term cycling performance of Fe$_3$Se$_4$/CoSe-C electrode at the current density of 5 A g^{-1}. d) GITT profiles of Fe$_3$Se$_4$/CoSe-C electrode. e) The calculated diffusion coefficients of Fe$_3$Se$_4$-C, CoSe-C, and Fe$_3$Se$_4$/CoSe-C electrodes during discharge and charge process. f) CV curves of Fe$_3$Se$_4$/CoSe-C electrode at various scan rates ranging from 0.1 to 2.0 mV s^{-1}. g) The b-value plotted against voltage of the Fe$_3$Se$_4$/CoSe-C electrode for cathodic scans. h) The charge-discharge profiles of Fe$_3$Se$_4$/CoSe-C||NVP full cell at a current density of 0.5 A g$^{-1}{}_{\text{anode}}$, and i) the corresponding cycling performance.

whole reaction process, the following equation can be used to calculate:[49]

$$i = k_1 v + k_2 v^{1/2} \tag{3}$$

where $k_1 v$ is the capacitive contribution and $k_2 v^{1/2}$ is the diffusion control contribution. Figure S11 (Supporting Information) illustrates the capacitance contribution of the entire CV at a scan rate of 0.5 mV s^{-1}. Approximately 68.9% of the charge storage is attributed to the pseudocapacitance behavior, as indicated by the red region, while the diffusion behavior primarily occurs around the redox peak. CV tests were conducted on the Fe$_3$Se$_4$-C and CoSe-C electrodes for comparison at the same scan rate (0.1–2.0 mV s^{-1}), as depicted in Figure S12 (Supporting Information). According to calculations, at the scan rate of 0.5 mV s^{-1}, the contribution rate of pseudocapacitance for Fe$_3$Se$_4$-C and CoSe-C is 59.8% and 64.9%, respectively. These values are lower than that of the Fe$_3$Se$_4$/CoSe-C electrode. In addition, we computed the ratio of pseudocapacitance at various scanning rates, as illustrated in Figure S13 (Supporting Information). As the scanning rate increases, the contribution of pseudocapacitance increases for all the as-prepared electrodes. Notably, the proportion of pseudocapacitance is higher in the Fe$_3$Se$_4$/CoSe-C heterostructures compared to pure Fe$_3$Se$_4$-C and CoSe-C at the same scan rate.

For practical applications, we utilized commercial Na$_3$V$_2$(PO$_4$)$_3$ (NVP) as the cathode material and synthesized Fe$_3$Se$_4$/CoSe-C as the anode material to assemble full cells. The assembled full cells were tested within a voltage range of 0.01–3.0 V. The specific capacity of the full cell was calculated based on the mass loading of the Fe$_3$Se$_4$/CoSe-C anode materials. As shown in Figure 3h, the Fe$_3$Se$_4$/CoSe-C||NVP full cell exhibits specific capacities of 340 and 270 mAh g$^{-1}{}_{\text{anode}}$ during the first charge and discharge cycles at a current density of 0.5 A g$^{-1}{}_{\text{anode}}$, corresponding to an initial Coulombic efficiency

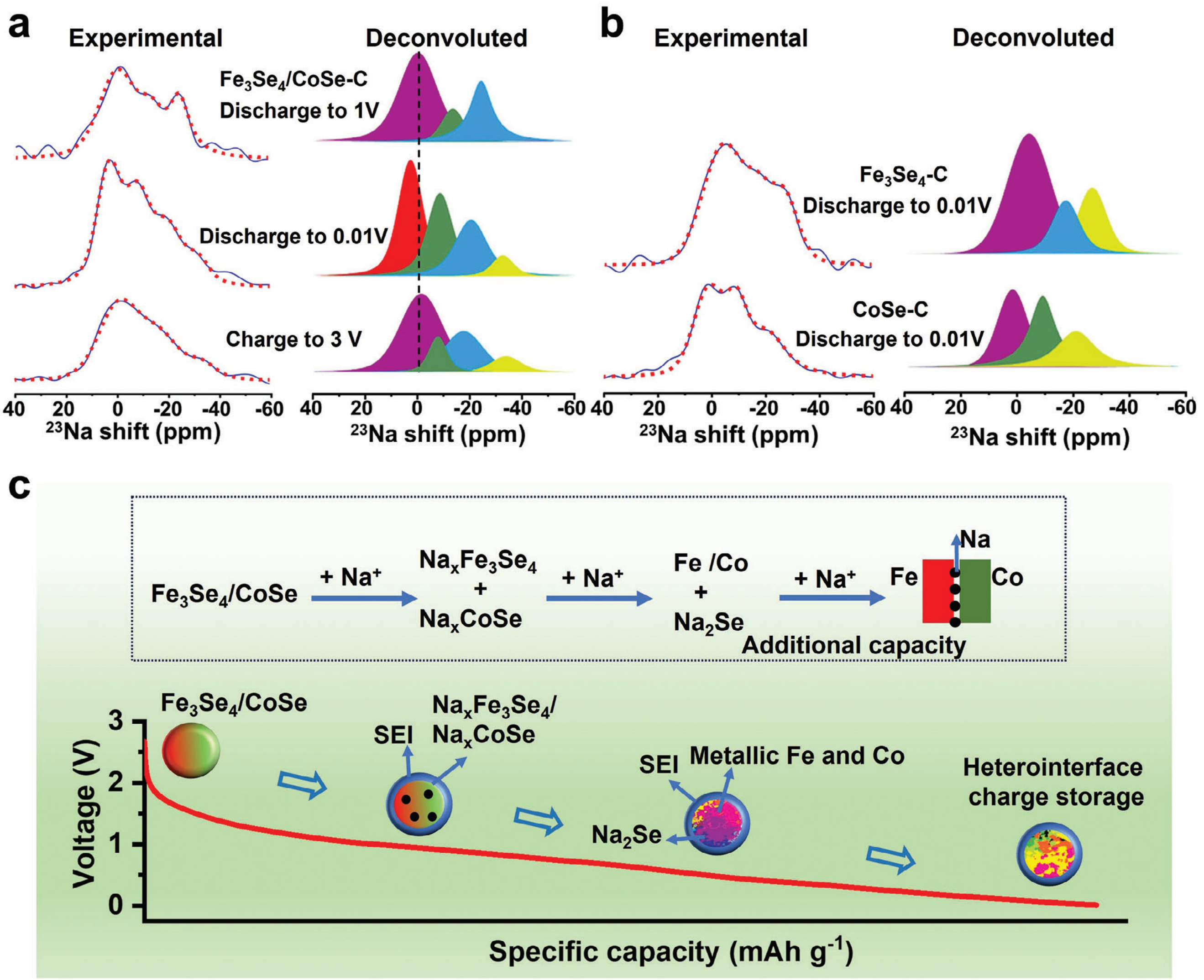

Figure 4. a) Experimental and simulated ^{23}Na NMR spectra of Fe_3Se_4/CoSe-C electrode at different discharge and charge stages. b) Experimental and simulated ^{23}Na NMR spectra of Fe_3Se_4-C electrode and CoSe-C electrode discharged to 0.01 V. c) The schematic of the sodium storage mechanisms at different stages for the Fe_3Se_4/CoSe heterogeneous.

of 79%. In addition, Figure 3i exhibits the cycling performance of the Fe_3Se_4/CoSe-C||NVP full cell at a current density of 0.5 A g^{-1}. The capacity decrease in the initial few cycles is likely due to the formation of SEI. After that, the specific capacity stabilizes ≈250 mAh g$^{-1}{}_{\text{anode}}$, indicating good stability and durability of the Fe_3Se_4/CoSe-C anode material during cycling. The Coulombic efficiencies show significant fluctuations during the initial few cycles, possibly due to charge loss associated with the formation of stable SEI. Nevertheless, in the subsequent cycles, the Coulombic efficiencies quickly recovered and stabilized at ≈99%. This high Coulombic efficiency demonstrates the good reversibility of the full cell during the charge and discharge processes.

To investigate the origin of the high capacity obtained by the as-prepared Fe_3Se_4/CoSe-C electrode, ex situ solid-state nuclear magnetic resonance (NMR) spectroscopy was conducted. **Figure 4a** depicts the ^{23}Na spectra of the Fe_3Se_4/CoSe-C electrode during the initial discharge and charge process. Additionally, the reference Fe_3Se_4 and CoSe electrodes were tested after discharge to 0.01 V for comparison (Figure 4b). For the Fe_3Se_4 electrode, three distinct peaks can be observed after full discharge. The peak at −5 ppm corresponds to Na$^+$ ions in the solid electrolyte interphase (SEI); the peak at −17 ppm mainly arises from Na$^+$ ions inserted into the active materials; and the peak at −26 ppm is attributed to Na$^+$ ions adsorbed on the surface of metallic Fe due to the space-charge effects.[50] Similarly, when the CoSe electrode is discharged to 0.01 V, three distinct peaks can be observed as well, showing properties analogous to those of the Fe_3Se_4 electrode. In contrast, in the case of the Fe_3Se_4/CoSe-C heterostructure, three peaks are observed after discharge to 1.0 V, where the peak at 0 ppm corresponds to Na$^+$ ions in the SEI, and the other two peaks correspond to Na$^+$ ions inserted into CoSe and Fe_3Se_4 phases, respectively. At this stage, the Na$^+$ ion adsorption onto Fe or Co is not detected because the conversion reaction has not

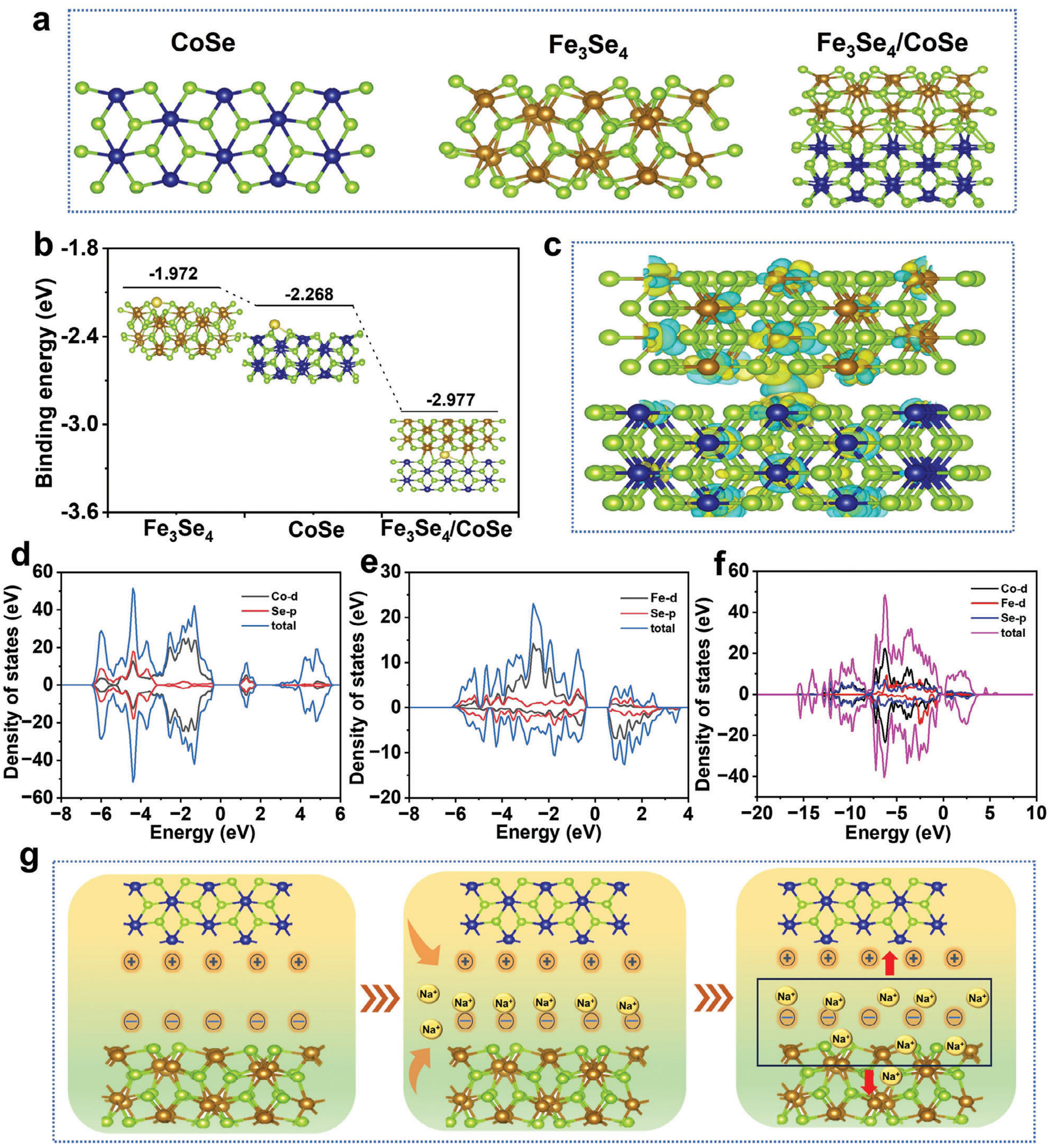

Figure 5. a) The CoSe, Fe_3Se_4, and Fe_3Se_4/CoSe heterostructure models. b) The adsorption energies of Na on CoSe, Fe_3Se_4, and Fe_3Se_4/CoSe heterostructure. c) 3D contour plot of charge density difference in Na adsorption at Fe_3Se_4/CoSe heterostructure. d–f) The corresponding density of states of d) CoSe, e) Fe_3Se_4, and f) Fe_3Se_4/CoSe heterostructure. g) Schematic illustration of the induced built-in electric field in the Fe_3Se_4/CoSe hetero interface for fast Na^+ ion diffusion.

yet occurred at this discharge state. As the discharge process continues to 0.01 V, significant changes in peak shape are observed. In addition to the peaks of Na^+ ion insertion into bulk materials and adsorbed on the surface of metallic Fe and Co, a new peak at 4 ppm appears (red portion), representing Na^+ ions stored at the heterojunction interface. In this state, the peak attributed to SEI is barely discernible due to being obscured, mirroring findings reported in the literature.[51] Upon charging the Fe_3Se_4/CoSe-C electrode to 3.0 V, the peak corresponding to Na^+ ion storage in the SEI returns to 0 ppm, and the peak at the heterojunction interface disappears, indicating the excellent reversibility of Na^+ ions storage behaviors at the heterojunction interfaces. The NMR results explain the high capacity and excellent cycling stability exhibited by the Fe_3Se_4/CoSe-C electrode in SIBs.

The summary of the electrochemical reaction process during the initial charge and discharge cycle is depicted in Figure 4c. The initial discharge processes involve the insertion of Na^+ ions and the generation of SEI films, contributing to the capacity in the high voltage range. When the discharge voltage drops below 1.0 V, a conversion reaction occurs, yielding metallic Fe and Co. Due to the space charge effect, some Na^+ ions are adsorbed onto the surface of metallic Fe or Co nanoparticles. Simultaneously, the heterogeneous interface formed by metallic Fe and Co also serves as active sites for Na^+ ion adsorption. Correspondingly, the charge and discharge curves of the Fe_3Se_4/CoSe-C electrode show the exceptionally high additional capacity primarily originates from the low-voltage range, where the active sites formed by the heterogeneous interface adsorb extra Na^+ ions.

To unveil the outstanding dynamic traits of heterogeneous structures theoretically, the density functional theory (DFT) study was employed. Initially, Fe_3Se_4 (001) and CoSe (001) surfaces were utilized to construct heterogeneous structures in Fe_3Se_4/CoSe (**Figure 5**a). The calculated formation energy of the Fe_3Se_4/CoSe heterostructure (−0.42 eV) attests to its thermodynamic stability. To assess the activity of the heterogeneous interface, the adsorption energies of Fe_3Se_4, CoSe, and Fe_3Se_4/CoSe for Na^+ ions were calculated (Figure 5b). The binding energy (E_b) was determined using the formula $E_b = E_{host+Na}$-E_{host}-E_{Na}, where $E_{host+Na}$ represents the energy of the adsorption system, while E_{Na} and E_{host} denote the energy of pure Na metal and the host system, respectively. A more negative E_b value indicates a stronger adsorption capacity for Na^+ ions. Structural optimization revealed that Na atoms tend to occupy metal positions and coordinate with four adjacent Se atoms to form Na-Se bonds. Based on this configuration, the adsorption energy of Na^+ ions in the Fe_3Se_4/CoSe heterostructure was calculated to be −2.97 eV, surpassing that of individual Fe_3Se_4 (−1.972 eV) and CoSe (−2.268 eV). The concise electronic structure analysis was performed to elucidate the charge transfer dynamics in detail, as depicted in Figure 5c. It is evident that the charge distribution primarily occurs at the interface region, with electron accumulation on the Fe_3Se_4 side and hole accumulation on the CoSe site during the sodium adsorption process.

Electronic conductivity is paramount in determining the electrochemical performance of anode materials. Therefore, a comprehensive examination of the electronic structure involves calculating the density of states (DOS) for various structural configurations, as illustrated in Figure 5d,e. Notably, CoSe exhibits a bandgap of 1.78 eV, while Fe_3Se_4 displays a bandgap of 1.33 eV, indicating their inherent semiconductive nature. Upon constructing the heterostructure, Fe_3Se_4/CoSe, an intriguing phenomenon emerges wherein the band structure successfully spans the Fermi level due to electron transfer from the Fe atom. Consequently, a diminished bandgap of 0.62 eV is observed, resulting in enhanced conductivity. These findings underscore the importance of heterostructure formation in Fe_3Se_4/CoSe for augmenting overall electronic conductivity. As illustrated in Figure 5g, prior to contact, the Fermi level of CoSe exceeds that of Fe_3Se_4. Consequently, upon contact between CoSe and Fe_3Se_4, an internal electric field arises at the heterogeneous interface. This leads to the accumulation of a negative charge on the Fe_3Se_4 side, while a positive charge accumulates on the CoSe side, resulting in an internal electric field directed from Fe_3Se_4 to CoSe. Facilitated by this electric field, the negative charge on the surface of Fe_3Se_4 attracts Na^+ ions to neutralize, thereby facilitating the diffusion of Na^+ within the heterogeneous structure.

3. Conclusion

In summary, we propose a sol-gel and selenization method for the controllable synthesis of Fe_3Se_4/CoSe heterostructures embedded within a 3D porous carbon-based structure. This superstructure not only shortens the ion diffusion path but also effectively mitigates the stress generated during the repetitive insertion and extraction of Na^+ ions, thereby ensuring the integrity of the interface. Theoretical calculations corroborate that this stable heterogeneous interface, characterized by atomic-scale binding, accelerates reaction kinetics and enhances charge transfer efficiency. Additionally, as evidenced by NMR observation, the heterointerface between Fe_3Se_4 and CoSe provides additional active sites for Na^+ ion storage, resulting in increased specific capacities. Leveraging this superior structural design, the Fe_3Se_4/CoSe-C heterostructure exhibits impressive magnification performance and exceptional cycle stability. At a high current density of 7 A g^{-1}, the Fe_3Se_4/CoSe-C electrode achieves a reversible specific capacity of 218 mAh g^{-1}. Even after 1000 cycles at a current density of 5 A g^{-1}, the Fe_3Se_4/CoSe-C electrode maintains a notable reversible specific capacity of 258 mAh g^{-1}. This study presents significant insights into interface engineering, offering innovative strategies for the development of high-performance conversion anode materials.

Supporting Information

Supporting Information is available from the Wiley Online Library or from the author.

Acknowledgements

C.M. and X.T. contributed equally to this work. C.R.M. acknowledges financial support from the Shandong Taishan Scholars Project (NO.ts20190932) and Youth Innovation Team Project of Shandong Provincial Education Department (No. 2022KJ143). G.X.W. would like to thank the financial support from the Australian Research Council (ARC) through the ARC Discovery Project (DP240102176), and B. S. would like to thank the financial support from ARC through the ARC Future Fellowship (FT220100561).

Open access publishing facilitated by University of Technology Sydney, as part of the Wiley - University of Technology Sydney agreement via the Council of Australian University Librarians.

Conflict of Interest

The authors declare no conflict of interest.

Data Availability Statement

The data that support the findings of this study are available from the corresponding author upon reasonable request.

Keywords

anode materials, DFT calculation, heterostructures, sodium ion batteries, transition metal selenides

Received: July 18, 2024
Revised: August 11, 2024

[1] L. Fang, N. Bahlawane, W. Sun, H. Pan, B. B. Xu, M. Yan, Y. Jiang, *Small* **2021**, *17*, 2101137.

[2] Y. Jiang, M. Xie, F. Wu, Z. Ye, Y. Zhang, Z. Wang, Y. Zhou, L. Li, R. Chen, *Small* **2021**, *17*, 2102893.

[3] Y.-J. Lei, X. Lu, H. Yoshikawa, D. Matsumura, Y. Fan, L. Zhao, J. Li, S. Wang, Q. Gu, H.-K. Liu, S.-X. Dou, S. Devaraj, T. Rojo, W.-H. Lai, M. Armand, Y.-X. Wang, G. Wang, *Nat. Commun.* **2024**, *15*, 3325.

[4] S. Jia, S. Kumakura, E. McCalla, *Energy Environ. Sci.* **2024**, *17*, 4343.

[5] C. Che, F. Wu, Y. Li, Y. Li, S. Li, C. Wu, Y. Bai, *Adv. Mater.* **2024**, *18*, 2402291.

[6] H. Au, H. Alptekin, A. C. S. Jensen, E. Olsson, C. A. O'Keefe, T. Smith, M. Crespo-Ribadeneyra, T. F. Headen, C. P. Grey, Q. Cai, A. J. Drew, M.-M. Titirici, *Energy Environ. Sci.* **2020**, *13*, 3469.

[7] P. Bai, Y. He, X. Zou, X. Zhao, P. Xiong, Y. Xu, *Adv. Energy Mater.* **2018**, *8*, 1703217.

[8] X. Chen, J. Tian, P. Li, Y. Fang, Y. Fang, X. Liang, J. Feng, J. Dong, X. Ai, H. Yang, Y. Cao, *Adv. Energy Mater.* **2022**, *12*, 2200886.

[9] X. Chen, C. Liu, Y. Fang, X. Ai, F. Zhong, H. Yang, Y. Cao, *Carbon Energy* **2022**, *4*, 1133.

[10] Y. Jiang, Y. Wang, G. Cheng, Y. Li, L. Dai, J. Zhu, W. Meng, J. Xi, L. Wang, Z. He, *Carbon Energy* **2024**, *6*, 2537.

[11] Z. Tang, S. Zhou, Y. Huang, H. Wang, R. Zhang, Q. Wang, D. Sun, Y. Tang, H. Wang, *Electrochem. Energy Rev.* **2023**, *6*, 8.

[12] J. Chen, X. Fan, X. Ji, T. Gao, S. Hou, X. Zhou, L. Wang, F. Wang, C. Yang, L. Chen, C. Wang, *Energy Environ. Sci.* **2018**, *11*, 1218.

[13] Y.-H. Kim, J.-H. An, S.-Y. Kim, X. Li, E.-J. Song, J.-H. Park, K. Y. Chung, Y.-S. Choi, D. O. Scanlon, H.-J. Ahn, J.-C. Lee, *Adv. Mater.* **2022**, *34*, 2201446.

[14] Y. Zeng, Z. Lin, Y. Meng, Y. Wang, M. Yu, X. Lu, Y. Tong, *Adv. Mater.* **2016**, *28*, 9188.

[15] Y. Li, Y. Guo, K. You, C. Guo, C. Li, X. Zeng, W. Wang, Q. Tang, Y. Yuan, *Prog. Nat. Sci.: Mater. Int.* **2023**, *33*, 92.

[16] M. Yang, X. Chang, L. Wang, X. Wang, M. Gu, H. Huang, L. Tang, Y. Zhong, H. Xia, *Adv. Mater.* **2023**, *35*, 2208705.

[17] D. Yu, K. Guo, F. Hou, Y. Zhang, X. Ye, Y. Zhang, P. Ji, U. Khalilov, G. Wang, X. Zhang, K. Wang, Y. Song, X. Zhong, H. Sun, J. Zhu, J. Liang, H. Wang, *Small* **2024**, *20*, 2312167.

[18] L. Wang, J. Zhu, N. Li, Z. Zhang, S. Zhang, Y. Chen, J. Zhang, Y. Yang, L. Tan, X. Niu, X. Wang, X. Ji, Y. Zhu, *Energy Environ. Sci.* **2024**, *17*, 3470.

[19] C. Hui, W. Fei, F. Huiyan, L. Zhendong, Z. Chengzhi, L. Anbang, Z. Xi, L. Qiuhong, L. Quanbing, T. Jun, *J. Mater. Chem. A* **2024**, *12*, 11266.

[20] Z.-H. Sun, D.-Y. Qu, D.-X. Han, Z.-Y. Gu, J.-Z. Guo, X.-X. Zhao, Y.-M. Ma, B.-L. Zhao, Z.-Q. Song, X.-L. Wu, L. Niu, *Adv. Mater.* **2023**, *36*, 2308987.

[21] T. Bashir, S. Zhou, S. Yang, S. A. Ismail, T. Ali, H. Wang, J. Zhao, L. Gao, *Electrochem. Energy Rev.* **2023**, *6*, 5.

[22] T. Zheng, P. Hu, Z. Wang, T. Guo, *Adv. Mater.* **2023**, *35*, 2306577.

[23] J. Chen, A. Pan, Y. Wang, X. Cao, W. Zhang, X. Kong, Q. Su, J. Lin, G. Cao, S. Liang, *Energy Storage Mater.* **2018**, *21*, 97.

[24] Y. T. Liu, P. Zhang, N. Sun, B. Anasori, Q. Z. Zhu, H. Liu, Y. Gogotsi, B. Xu, *Adv. Mater.* **2018**, *30*, 1707334.

[25] K. Zhang, M. Park, L. Zhou, G.-H. Lee, J. Shin, Z. Hu, S.-L. Chou, J. Chen, Y.-M. Kang, *Angew. Chem., Int. Ed.* **2016**, *55*, 12822.

[26] Y. T. Liu, P. Zhang, N. Sun, B. Anasori, Q. Z. Zhu, H. Liu, Y. Gogotsi, B. Xu, *Adv. Mater.* **2023**, *13*, 2203523.

[27] X. Song, X. Li, H. Shan, J. Wang, W. Li, K. Xu, K. Zhang, H. M. K. Sari, L. Lei, W. Xiao, J. Qin, C. Xie, X. Sun, *Adv. Funct. Mater.* **2024**, *34*, 23032011.

[28] F. Chen, S. J. Robertson, X. Xu, S. Chen, C. Sun, M. Shao, J. Wang, *Nano Energy* **2024**, *123*, 109414.

[29] J. Cao, J. Li, D. Li, Z. Yuan, Y. Zhang, V. Shulga, Z. Sun, W. Han, *Nano-Micro Lett.* **2021**, *13*, 113.

[30] Y. P. Deng, Z. G. Wu, R. Liang, Y. Jiang, D. Luo, A. Yu, Z. Chen, *Adv. Funct. Mater.* **2019**, *29*, 1808522.

[31] P. Liu, J. Han, K. Zhu, Z. Dong, L. Jiao, *Adv. Energy Mater.* **2020**, *10*, 2000741.

[32] Q. Pan, Q. Zhang, F. Zheng, Y. Liu, Y. Li, X. Ou, X. Xiong, C. Yang, M. Liu, *ACS Nano* **2018**, *12*, 12578.

[33] Y. Xi, X. Wang, H. Wang, M. Wang, G. Wang, J. Peng, N. Hou, X. Huang, Y. Cao, Z. Yang, D. Liu, X. Pu, G. Cao, R. Duan, W. Li, J. Wang, K. Zhang, K. Xu, J. Zhang, X. Li, *Adv. Funct. Mater.* **2024**, *34*, 2309701.

[34] T. He, W. Zhao, J. Hu, C. Deng, D. Yan, S. Huang, *Adv. Funct. Mater.* **2023**, *34*, 2310256.

[35] J. Cao, Z. Sun, J. Li, Y. Zhu, Z. Yuan, Y. Zhang, D. Li, L. Wang, W. Han, *ACS Nano* **2021**, *15*, 3423.

[36] C. Shang, L. Hu, D. Luo, K. Kempa, Y. Zhang, G. Zhou, X. Wang, Z. Chen, *Adv. Sci.* **2020**, *7*, 2002358.

[37] Y. Zheng, T. Zhou, C. Zhang, J. Mao, H. Liu, Z. Guo, *Angew. Chem., Int. Ed.* **2016**, *55*, 3408.

[38] D. Kang, Q. Liu, M. Chen, J. Gu, D. Zhang, *ACS Nano* **2015**, *10*, 889.

[39] Y. Wang, Y. Zhang, R. Shao, Q. Guo, *Chem. Eng. J.* **2022**, *442*, 136362.

[40] H. Ma, Z. Wan, J. Li, R. Wu, Z. Zhang, B. Li, B. Zhao, Q. Qian, Y. Liu, Q. Xia, G. Guo, X. Duan, X. Duan, *Adv. Mater.* **2019**, *31*, 1900901.

[41] P. Li, T. Huang, Y. Lou, H. He, X. Tang, Y. Cai, M. Zhang, *J. Energy Storage* **2023**, *78*, 109951.

[42] W. Zhao, X. Ma, L. Yue, L. Zhang, Y. Luo, Y. Ren, X.-E. Zhao, N. Li, B. Tang, Q. Liu, Y. Liu, S. Gao, A. A. Alshehri, X. Sun, *J. Mater. Chem. A* **2022**, *10*, 4087.

[43] W. Yang, S. Zihan, H. Junfeng, Z. Huigang, Z. Qingshan, *Adv. Energy Mater.* **2023**, *13*, 2204345.

[44] W. Wang, X. Wang, J. Shan, L. Yue, Z. Shao, L. Chen, D. Lu, Y. Li, *Energy Environ. Sci.* **2023**, *16*, 2669.

[45] P. Zhang, J. Fan, Y. Wang, Y. Dang, S. Heumann, Y. Ding, *Carbon* **2024**, *222*, 118998.

[46] M. Ren, H. Zang, S. Cao, W. Liu, M. Li, J. Yao, F. Cai, J. Cui, Y. Wang, *J. Energy Storage* **2024**, *81*, 110486.

[47] J. S. Horner, G. Whang, D. S. Ashby, I. V. Kolesnichenko, T. N. Lambert, B. S. Dunn, A. A. Talin, S. A. Roberts, *ACS Appl. Energy Mater.* **2021**, *4*, 11460.

[48] J. Wang, J. Polleux, J. Lim, B. Dunn, *J. Phys. Chem. C* **2007**, *111*, 14925.

[49] M. Forghani, A. P. Cameron, S. W. Donne, *J. Electrochem. Soc.* **2021**, *168*, 050503.

[50] Q. Li, H. Li, Q. Xia, Z. Hu, Y. Zhu, S. Yan, C. Ge, Q. Zhang, X. Wang, X. Shang, S. Fan, Y. Long, L. Gu, G.-X. Miao, G. Yu, J. S. Moodera, *Nat. Mater.* **2020**, *20*, 76.

[51] C. Ma, X. Li, C. Deng, Y.-Y. Hu, S. Lee, X.-Z. Liao, Y.-S. He, Z.-F. Ma, H. Xiong, *ACS Nano* **2019**, *13*, 671.